Meccanica (2023) 58:981–1001
https://doi.org/10.1007/s11012-023-01654-5

An experimental procedure for the identification of the dynamic parameters for the rigid-ring tyre model

Matteo Massaro · Matteo Mottola · Elvio Bonisoli · Domenico Lisitano

Received: 5 July 2022 / Accepted: 10 March 2023 / Published online: 25 April 2023

Abstract Several approaches have been developed over the years for the modelling of the tyre behaviour in vehicle-dynamic applications. The so-called 'rigid-ring' models are among the classics for the modelling of the belt dynamics. Although there are several works dealing with the vibrating properties of tyres, the problem of the identification of the related rigid-ring model parameters has not been described other than qualitatively or partially. The aim of this work is thus to fill this gap and to devise a procedure for the experimental characterisation of such parameters, namely the frequency and damping of the in-plane and out-of-plane belt vibration modes as well as the associated masses and inertias. An experimental modal analysis (EMA) approach is employed, which involves an instrumented hammer combined with three-axial accelerometers roving on 16 stations equally spaced along the tyre circumference. The method is numerically demonstrated on the finite-element models of a motorcycle tyre and a car tyre. The approach is also experimentally validated on a real tyre. The rigid-ring vibration modes of the motorcycle tyre are in the range 70–220 Hz, while those of the car tyre are in the range 51–85 Hz. The ratios of the mass/inertia of the rigid ring to the mass/inertia of the tyre are in the range 40–87% and 68–74% for the motorcycle and car respectively.

Keywords Tyre · EMA · Rigid-ring · MF-swift · Motorcycle · Car · Vehicle · Vibration

M. Massaro (✉) · M. Mottola
Department of Industrial Engineering, University of Padova, Via Venezia 1, 35131 Padua, Italy
e-mail: matteo.massaro@unipd.it

E. Bonisoli · D. Lisitano
Department of Mechanical and Aerospace Engineering, Politecnico di Torino, Corso Duca degli Abruzzi 24, 10124 Turin, Italy

1 Introduction

Tyre models which provides forces and torques as a function of slips and loads are commonly used in vehicle dynamics applications [1–8]. Tyre models may be classified in three main levels of complexity: basic, neglecting the belt inertia [9–12], suitable for simulations with frequencies up to approximatively 15 Hz and wavelength greater than approximatively 1.5 m, intermediate, considering the belt as a rigid ring elastically mounted on the rim [13–15], suitable for simulations up to 60–100 Hz and wavelength greater than 0.1-0.2 m, and advanced, allowing belt deflection [16–19], suitable for higher frequencies and shorter wavelengths. Finally, there are also models dedicated to the investigation of specific issues, such as tyre-temperature distribution [20], tyre wear [21], contact pressure [22, 23], impulsive loading [24], hydroplaning [25, 26].

This works focuses on intermediate models, and in particular on the belt vibration modes that need

be identified to populate such rigid-ring models. The belt, assumed rigid, has six degrees of freedom (DOF) with respect to the rim. The corresponding vibration modes are named longitudinal, vertical, torsional (or wind-up), lateral, camber and yaw. Under the assumptions that the tyre is axial-symmetric and lifted from the ground, the former three modes are in-plane and the latter three modes are out-of-plane. In addition, the longitudinal and vertical modes have the same frequency, as well as the camber and yaw modes. Therefore, there are four main modes that need be identified, two of which with multiplicity two. Of course the characteristics of such modes may change with temperature, inflation pressure, etc. However, most of the procedures proposed for their analysis can potentially be applied with the tyre in different conditions.

A number of works dealing with the vibration modes of tyres are documented in the literature. The most relevant to this work are those dealing with vehicle-dynamic applications [1–19], rather than those focusing on stress and fatigue estimations.

An example of the typical in-plane modes of car tyres is reported in [5], the first of which consists of a vertical oscillation of the belt (without distortion)—no details are given regarding the boundary conditions considered. The experimental modal analysis of a suspended passenger-car tyres under radial and tangential excitations is discussed in [27]. It is found that the natural frequencies increases with the inflation pressure, while the damping decreases. In [28] a flexible-ring model is presented, which is then simplified into a rigid-ring model. The focus is on the in-plane dynamics. The modal testing of a fixed tyre and a free tyre, both suspended from the ground, is also included, finding a torsional and a vertical modes with minor belt distortion—the frequencies are higher in the free condition. The application of ring models for the simulation of the tyre dynamics on uneven roads is considered in [15]. Modal tests are performed on the tyre loaded on the ground and with a pinned axle. The free tyre vs. tyre standing on the road conditions are further compared in [29], with a review of the past relevant literature. Impulsive testing on the non-rotating tyre are applied, with sensors being mounted on the belt and rim to monitor the tangential and radial directions. The rigid-ring model is extended to include also the out-of-plane dynamics in [30]. The experimental validation includes modal tests of a car tyre loaded against the ground with the axle pinned. The tyre modes are further discussed in [2], by means of a numerical tyre model. In unloaded condition, with pinned axle, the in-plane modes are the vertical/longitudinal (which are coincident) modes and the torsional mode, while the out-of-plane modes are the lateral and yaw/camber (which are coincident). In loaded conditions (assuming contact with a drum), and pinned axle, neither the vertical/longitudinal nor the yaw/camber modes are coincident anymore.

A time domain approach to identify the modal parameters of the in-plane ring-model of car tyres is presented in [31]: the inertia are identified using a torsional pendulum, while the natural frequencies and damping are obtained from the time histories of the longitudinal and vertical hub forces during a passing-over-cleat test, with the hub held fixed. The time-domain procedure can also be employed for out-of-plane tests, while passing-over-cleat under an angle [32]. Excitation of a loaded car tyre with shaker is carried out in [33], the focus being again on in-plane modes for NVH investigations. Both impulsive and shaker excitations are considered in [34], with a discussion on the common issues faced when testing tyres. In [35] the in-plane modes of a truck tyre are investigated using a shaker on a seismic table, with a focus on the damping identification. It is shown that the proportional damping is not a good assumption at high frequencies.

In [36] an experimental modal analysis on two scooter and two motorcycle tyres is carried out at different inflation pressures, finding that the first out-of-plane mode is the camber mode, followed by the lateral mode – of course the frequencies are rising with the inflation pressure. An impulsive modal approach was employed. The rim of the tyre was fixed to a stiff column, and a roving-hammer technique applied, the excitation being given to the belt in the lateral direction. The tyre is unloaded. The investigation is extended in [37] to include two more motorcycle tyres: the results and frequency ranges are confirmed. The effect of rolling speed on the in-plane modes of car tyres is considered in [38], where also the effect of inflation pressure and vertical load is discussed.

Finally, in [39] guidelines are given for the extraction of the frequencies of the lower-order vibration modes of tyres with a minimal set-up, consisting of one or two locations for the impacts and

accelerometers. The tyre is assumed rigidly supported at the spindle. Two loading conditions are considered: free tyre, i.e. with the tread not in contact with the ground, and loaded tyre, i.e. with the tread compressed against a surface to give the desired load. The mode type (e.g. lateral vs. yaw/camber) is identified from the inspection of the frequency response functions (FRF), e.g. position of the main peaks and related phases. The lateral modes provided for illustration purposes are at 35 and 52 Hz, the yaw/camber mode at 53 and 65 Hz, the torsion modes at 42 and 83 Hz, while the radial modes are at 66 and 90 Hz.

The perusal of the literature shows that most of the works published are focused on the in-plane vibration modes of car tyres, while the works related to out-of-plane modes are limited. The focus is most of the time on the frequencies and (sometimes) damping of the modes, while the masses and inertias associated to the modes are often not discussed. A number of different constraint conditions have been employed, e.g. free vs. fixed and loaded vs. unloaded, as well as different excitation methods, e.g. impulse vs. shaker. However, in the case of application of a rigid-ring model (see Fig. 1), e.g. the MF-Swift [14], the user is requested to specify the frequencies, damping and inertia of the belt for a tyre not in contact with the ground and with fixed rim [2, 13]. This is precisely the focus of this work. In general, it is expected that the mass and inertia associated to the belt are smaller than the actual mass and inertia of the belt, since the portion of belt in contact with the rim cannot move with respect to the rim and thus is not involved in the vibration.

This work has several objectives. The first is to devise a procedure for the identification of the dynamic parameters of rigid-ring tyre models (to be used in vehicle-dynamic applications), that can be experimentally carried out using general-purpose equipment for vibration analysis (Sect. 2). Such procedure can be applied both for the identification of the in-plane and out-of-plane dynamics, thus departing from most of the literature that focuses on in-plane dynamics only. The second is to demonstrate the proposed procedure on a ideal (numerical) environment, in order to clarify the application of the method and support the subsequent experimental findings on the real tyre (Sect. 3). Both a motorcycle tyre and a car tyre are considered, to demonstrate the generality of the approach. The third is to demonstrate the proposed procedure experimentally, in order to show that the method works in a real environment (Sect. 4). The fourth objective is to show the typical pattern of the tyre in-plane and out-of-plane FRF and to draw remarks related to the dynamic response of the finite-element tyre model, the real tyre and the rigid-ring tyre model, and to the assumptions enforced when employing rigid-ring tyre models (Sect. 5).

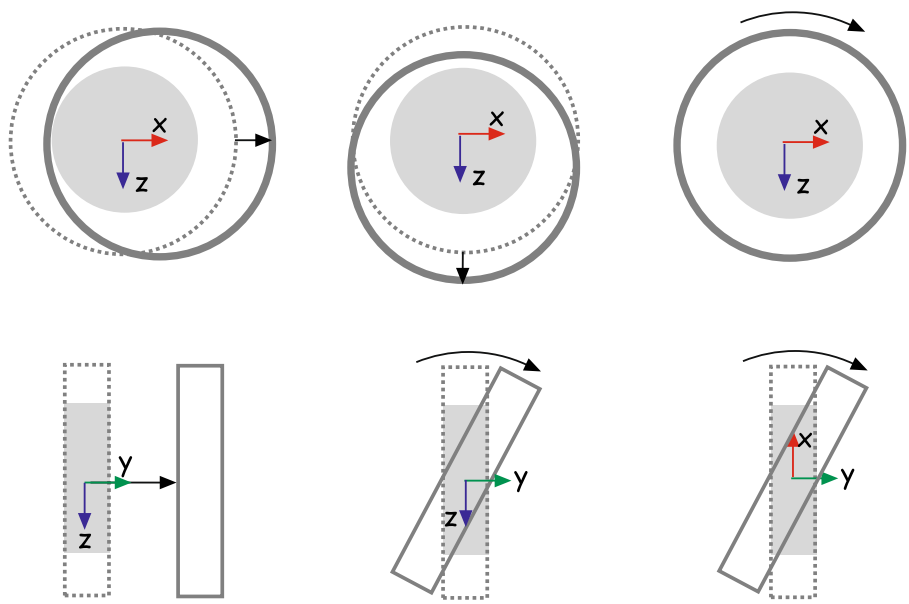

Fig. 1 Degrees of freedom of the rigid-ring (dark grey) with respect to the rim (light grey): longitudinal (top left), vertical (top centre), torsion (top right), lateral (bottom left), camber (bottom centre) and yaw (bottom right)

2 Method

The objective is the computation of the FRF of a tyre, which are then decomposed into modal components, with the aim of extracting the associated frequencies, damping ratios and inertias. The output of the FRF are the three-dimensional accelerations of a number of stations N along the external (rolling) circumference of the tyre belt. The inputs of the FRF are the impact forces in the tangential, radial and lateral directions. The underlining assumption, which is also the assumption of the rigid-ring models, is that the lower-order modes do not involve significantly the belt deflection, and that each mode involves significantly only one DOF of the rigid ring model, e.g. the lateral mode can be considered a pure lateral translation, with negligible contributions from the other five DOF of the ring.

The FRF of a M degree-of-freedom (MDOF) system can be written as the summation of the FRF of the single degree-of-freedom (SDOF) systems. The receptance (displacement over force) FRF $\boldsymbol{\alpha}_{\mathrm{jk}}$ representing the displacement at the DOF j when exciting the DOF k is given by [40, 41]

$$\boldsymbol{\alpha}_{\mathrm{jk}}(\omega) = \sum_{\mathrm{r}=1}^{M} \left[\frac{\boldsymbol{\psi}_{\mathrm{jr}} \boldsymbol{\psi}_{\mathrm{kr}}}{a_{\mathrm{r}}(\mathrm{i}\omega - s_{\mathrm{r}})} + \frac{\boldsymbol{\psi}^{*}_{\mathrm{jr}} \boldsymbol{\psi}^{*}_{\mathrm{kr}}}{a^{*}_{\mathrm{r}}\left(\mathrm{i}\omega - s^{*}_{\mathrm{r}}\right)} \right], \tag{1}$$

where $\mathrm{i} = \sqrt{-1}$, ω is the frequency, s_{r} is the r^{th} eigenvalue, $\boldsymbol{\psi}_{\mathrm{jr}}$ and $\boldsymbol{\psi}_{\mathrm{kr}}$ are the components of the r^{th} mode-shape eigenvector $\boldsymbol{\psi}_{\mathrm{r}}$ at DOF j and k respectively, while a_{r} is the modal constant and * represents the complex conjugate. The complex formulation for generic non-classical damping with conjugate pairs of eigenvectors and eigenvalues is adopted.

The modal model is obtained from the fit ting of the $3 \times N$ experimental FRF (x, y and z directions for each of the N stations where the sensors are placed), to obtain s_{r}, $\boldsymbol{\psi}_{\mathrm{r}}$ and a_{r} of (1). Different fitting techniques can be applied to extract the modal model. In this work the 'PolyMax' function within the Simcenter Testlab [42] is used, which is based on polyreference least-squares complex frequency-domain modal identification method. At this stage, the infinite dimension real system is fitted with a M-dimension model (in this work M is the number of relevant modes in the range 0–300 Hz). The choice of M is such that the difference between the experimentally measured FRF and the FRF obtained through (1) is minimum in the frequency range of interest. It goes without saying that it is straightforward to transform the measured inertance (acceleration over force) into the receptance used for the calculations, $-\omega^2$ being the conversion factor.

The following procedure is carried out in order to extract the inertias associated to each of the six rigid-ring vibration modes: (i) projection of synthesized $\boldsymbol{\alpha}^{\mathrm{r}}_{\mathrm{jk}}$ to the DOF of the rigid ring (lateral, longitudinal, vertical, camber, yaw, spin); (ii) computation of the average receptance $\bar{\boldsymbol{\alpha}}^{\mathrm{r}}_{\mathrm{jk}}$, after exclusion of the outliers (if any); (iii) fitting of $\bar{\boldsymbol{\alpha}}^{\mathrm{r}}_{\mathrm{jk}}$ with a SDOF model to find the related mass, the frequency and damping ratios being already known from the modal model.

The projection on the translational DOF—which is necessary to extract the lateral, longitudinal and vertical modes—is immediate, and consists in taking the signals in the proper direction (lateral, longitudinal, vertical). The projection of the rotational DOF—which is necessary to extract the camber, yaw and spin modes—is obtained by transformation of the displacement/force receptance in a rotation/torque receptance as follows:

$$\boldsymbol{\alpha}^{\mathrm{r}}_{\mathrm{jk}}\left[\frac{\mathrm{rad}}{\mathrm{Nm}}\right] = \frac{\boldsymbol{\alpha}^{\mathrm{r}}_{\mathrm{jk}}\left[\frac{\mathrm{m}}{\mathrm{N}}\right]}{d_{\mathrm{j}} d_{\mathrm{k}}}, \tag{2}$$

where d_{j} and d_{k} are the distances of the j^{th} and k^{th} node from the rotation axis of the rigid-ring. Such axis is obtained linking the structural nodes of yaw and camber modes, while it is assumed to coincide the hub axis for the torsional mode. A SDOF receptance is then obtained for each DOF of the rigid ring by computing the complex mean of the projected receptances. Finally, the magnitude of the obtained receptance may be rewritten with the classic

$$|\boldsymbol{\alpha}^{\mathrm{r}}(\omega)| = \frac{1}{m_{\mathrm{r}} \sqrt{(\omega_{\mathrm{r}}^2 - \omega^2)^2 + (2\zeta_{\mathrm{r}}\omega_{\mathrm{r}}\omega)^2}}, \tag{3}$$

where m_{r} is a mass or a moment of inertia, depending on the DOF involved, while $\omega_{\mathrm{r}} = |s_{\mathrm{r}}|$ and $\zeta_{\mathrm{r}} = -\mathrm{Re}(s_{\mathrm{r}})/\omega_{\mathrm{r}}$ are the natural frequency and damping ratio of the r^{th} mode. The only unknown is thus m_{r}, which is can be easily obtained.

3 Numerical test

The procedure described in Sect. 2 is preliminary tested on numerical tyre models, in order to have a perfectly axial-symmetric and noise-free system. The rationale is to verify that the procedure works on an ideal model and environment, before moving to experiments. Both a motorcycle tyre model and car tyre model are considered, in order to test the procedure on two quite different datasets. Both models are developed within Lupos [43, 44].

The finite-element model can be written in the standard form

$$\boldsymbol{M}\ddot{\boldsymbol{x}} + \boldsymbol{C}\dot{\boldsymbol{x}} + \boldsymbol{K}\boldsymbol{x} = \boldsymbol{0}, \tag{4}$$

where $\boldsymbol{M}, \boldsymbol{C}, \boldsymbol{K}$ are the mass, damping and stiffness matrix, while $\boldsymbol{x}$ is the vector of coordinates DOFs). Proportional damping, which is a special case of classical damping [45–47], is assumed and tuned to provide damping ratios consistent with those typical of tyres. The damping matrix is given by

$$\boldsymbol{C} = c_1\boldsymbol{M} + c_2\boldsymbol{K}, \tag{5}$$

where, in this case, $c_1 = 30$ rad/s and $c_2 = 0$ s/rad. The eigenproblem related to (4) provides the vibration modes, that are real as a consequence of the classical damping assumption.

The application of the identification procedure of Sect. 2 is carried out by the FRF obtained at the 16 equally spaced points along the circumference of the tyre; see Fig. 2. In general, the selected location of sensors should allow to properly monitor the shape of the vibration modes of interest. When it comes to the rigid-ring modes of the tyre, the selection is straightforward (e.g. the set employed in this work). In more complex scenarios, automatic selection methods such like MoGeSec [48] can be employed.

The FRFs are numerically obtained from the numerical mode-shapes through (1). The FRFs from the lateral force excitation (direction y) on the node 1 of Fig. 2 and the lateral motion of the 16 stations are used to extract the lateral modes and the yaw/camber modes. The FRFs from the vertical force excitation (direction z) on the node 1 of Fig. 2 and the vertical motion of the 16 stations are used to extract the vertical mode. The FRF from the tangential force excitation (direction x) on the node 1 of Fig. 2 and the tangential motion of the 16 stations are used to extract

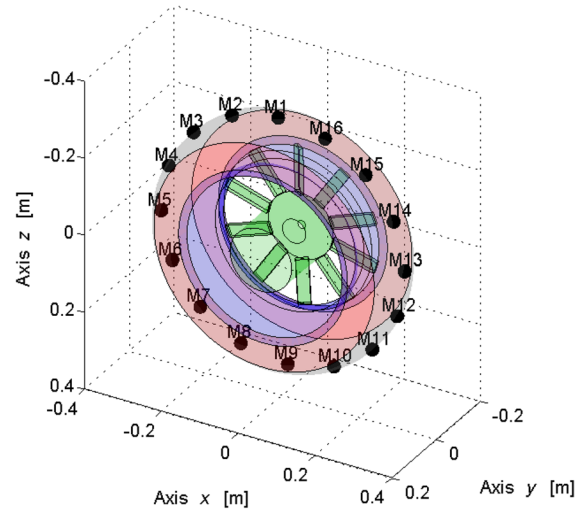

Fig. 2 Finite element model of the tyre with the 16 excitation/responses stations

the spin mode. Each set of FRF is used as an experimentally measured FRF. Therefore, they are initially fitted to obtain the modal model, i.e. $s_r, \boldsymbol{\psi}_r, a_r$.

The quality of the fitting is monitored using the correlation ρ and error ϵ between each pair of experimental FRF and modal model FRF. The correlation is defined as the normalized complex product of the fitted modal model FRF ($\boldsymbol{\alpha}_{jk}(\omega)$) and the experimental FRF ($\boldsymbol{\alpha}^e_{jk}(\omega)$)

$$\rho = \frac{\left|\sum_{\omega=\omega_1}^{\omega_2} \boldsymbol{\alpha}^e_{jk}(\omega)\boldsymbol{\alpha}^*_{jk}(\omega)\right|^2}{\left(\sum_{\omega=\omega_1}^{\omega_2} \boldsymbol{\alpha}^e_{jk}(\omega)\boldsymbol{\alpha}^{e*}_{jk}(\omega)\right)\left(\sum_{\omega=\omega_1}^{\omega_2} \boldsymbol{\alpha}_{jk}(\omega)\boldsymbol{\alpha}^*_{jk}(\omega)\right)} \tag{6}$$

in the frequency range $[\omega_1, \omega_2]$, while the error is defined as the least-square difference normalized to the experimental value

$$\epsilon = \frac{\sum_{\omega=\omega_1}^{\omega_2} \left(\boldsymbol{\alpha}_{jk}(\omega) - \boldsymbol{\alpha}^e_{jk}(\omega)\right)\left(\boldsymbol{\alpha}_{jk}(\omega) - \boldsymbol{\alpha}^e_{jk}(\omega)\right)^*}{\sum_{\omega=\omega_1}^{\omega_2} \boldsymbol{\alpha}^e_{jk}(\omega)\boldsymbol{\alpha}^{e*}_{jk}(\omega)}. \tag{7}$$

In this work $f_1 = \omega_1/2\pi = 15$ Hz and $f_2 = \omega_2/2\pi = 300$ Hz, while * represents the conjugate. Next, the FRF are projected on the rigid-ring DOF and averaged. Finally, the mass m_r associated to each SDOF model is computed. The intermediate steps of the procedure will be detailed for the

experimental tests, to avoid repetition and to keep the presentation concise.

3.1 Motorcycle tyre

The model consists of 170 one-dimensional beam and rod elements representing the wheel spokes and bead wires with additional 3360 one-dimensional lumped elastic and rigid connectors, 3040 two-dimensional four node shell element with different thickness and material for the wheel rim, hub, tyre sidewall and tyre tread, and 2800 three-dimensional hexahedral elements to model the inflated air; Fig. 2. Such numerical model is considered sufficiently representative for modelling the lower-order modes of a 16 inch 180/65 motorcycle tyre. The fixed constraint is reproduced by fixing the rim nodes to the ground. The total number of DOFs is 15,855. The mass of the tyre is 10.96 kg, the yaw/camber moment of inertia is 0.52 kg m^2, the spin moment of inertia is 0.95 kg m^2.

The shapes of the most relevant modes for this work are shown in Fig. 3, with the magnitude of the displacements increasing with colors from blue to red. The lateral mode has a frequency of 71 Hz (damping 3.4%) and is shown in Fig. 3a: the portion of belt close to the rim does not move (blue), while the portion of the belt along the external circumference moves almost like a rigid-ring in the lateral direction (red). The camber/yaw mode has a frequency of 99.4 Hz (damping 2.4%) and is shown in Fig. 3b. The rotation axis passes through the blue points (i.e. has direction lower-left to upper-right): the points of the belt around that axis do not move (blue), while those far from the axis have the maximum displacement (red). There is another mode at the same frequency (the tyre is perfectly axial-symmetric) with the rotation axis perpendicular to the one depicted in Fig. 3b. Obviously, all rotation axes can be obtained by the combination of these two modes. The torsion/spin mode has a frequency of 234.3 Hz (damping 1.0%) and is shown in Fig. 3c. The portion of the belt close to the rim does not move (blue), while portion around the rolling circumference has maximum displacement (red). Even in this case, belt distortions on the rolling portion of the belt are minimum, which moved like a rigid-ring Finally, a vertical mode at 217.2 Hz (damping 1.1%) is shown in Fig. 3d. The portion of the belt on top (and bottom—not visible in the figure) have the maximum displacement (red), while the portions on the sides have smaller displacement (green). There is another mode at the same frequency (the tyre is perfectly axial-symmetric): it is the longitudinal mode. Vibration along each radial direction can be obtained by combination of these two modes. The finite-element model has many other (higher order) modes, which are not relevant in this work because they involve significant carcass distortion, and are thus not suitable to fit a rigid-ring model.

When obtaining the modal model, the minimum fitting correlations for lateral and tangential excitations is 99.9%, while the maximum error is 0.1%. The fitting of the radial excitation dataset provides correlations greater than 99.6% and errors smaller than 0.4% for both radial and tangential directions, with the exception of the tangential directions of node 1 and 9 (i.e. normal to the excitation), which have correlations of 64% and 56% and errors of 36% and 44%, respectively. The identified masses and inertias are reported in Tab. 1, where m_r is the mass/inertia that is associated to the rigid ring, m is the total mass/inertia of the belt, while the last column represents the ratio between the two inertia.

It is worth stressing that, even in the ideal numerical model, the mass related to the lateral direction is not equal to the mass associated to the vertical/longitudinal direction. On the contrary, the masses associated to the vertical and longitudinal directions are the same because of tyre symmetry. The same reasoning applies to the inertias associated to the camber and yaw modes. When it comes to the practical implementation of the rigid-ring model, the user needs to decide for a single mass value, that will be assigned to the ring body. In addition, the difference between m and m_r is added to the rim, so that the total mass of the wheel remains the same.

3.2 Car tyre

The model consists of 128 one-dimensional rod elements representing rim welding points and bead wires with additional 1280 one-dimensional lumped elastic and rigid connectors, 1152 two-dimensional four node shell element with different thickness and material for the wheel rim, disk, tyre sidewall and tyre tread, and 1024 three-dimensional hexahedral elements to model the inflated air. Such numerical model is representative for modelling the lower-order modes of a 16 inch 205/55 car tyre. The fixed constraint is

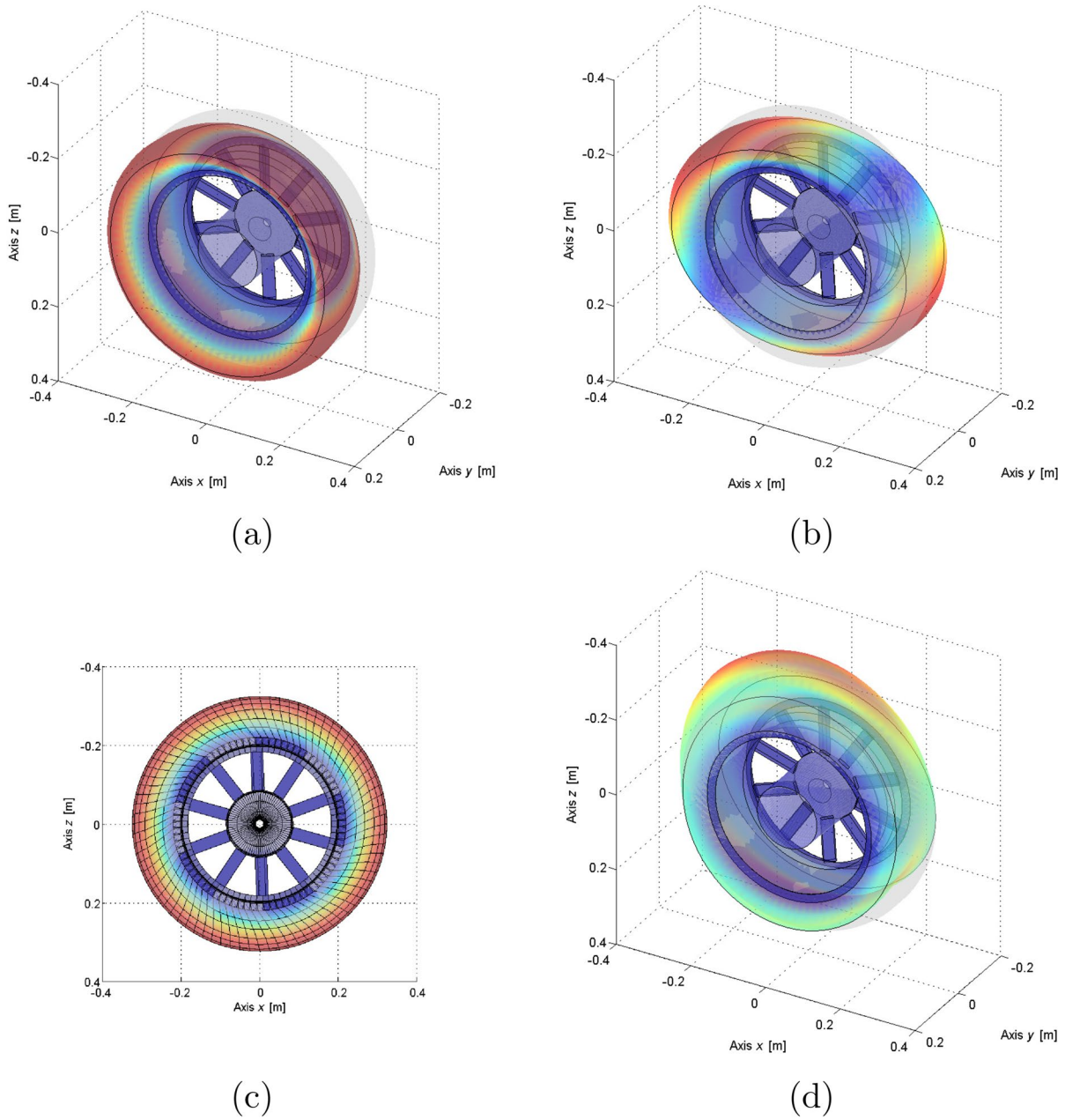

Fig. 3 Lateral (**a**), yaw/camber (**b**), torsion/spin (**c**) and vertical/longitudinal (**d**) modes of the motorcycle tyre finite-element model

Table 1 Parameters of the motorcycle tyre rigid-ring model, extracted from the finite-element model

Mode	f_r	ζ_r	m_r	m	m_r/m
Lateral	71.0 Hz	3.36%	8.90 kg	10.96 kg	0.81
Camber/yaw	99.4 Hz	2.40%	0.45 kg m^2	0.52 kg m^2	0.87
Torsional/spin	234.3 Hz	1.01%	0.76 kg m^2	0.95 kg m^2	0.80
Vertical/longitudinal	217.2 Hz	1.09%	4.38 kg	10.96 kg	0.40

reproduced by fixing the rim nodes to the ground. The total number of DOFs is 6324. The mass of the tyre is 8.05 kg, the yaw/camber moment of inertia is 0.35 kg m^2, the spin moment of inertia is 0.61 kg m^2.

The shapes of the most relevant modes for this work are shown in Fig. 4, with the magnitude of the displacements increasing with colors from blue to red. The lateral mode has a frequency of 51.4 Hz (damping 4.7%) and is shown in Fig. 4a: the portion of the belt close to the rim does not move (blue), while the portion of the belt along the external circumference moves almost like a rigid-ring in the lateral direction (red). The camber/yaw mode has a frequency of 54.3 Hz (damping 4.4%) and is shown in Fig. 4b. The rotation axis passes through the blue points (i.e. has direction left to right): the points of

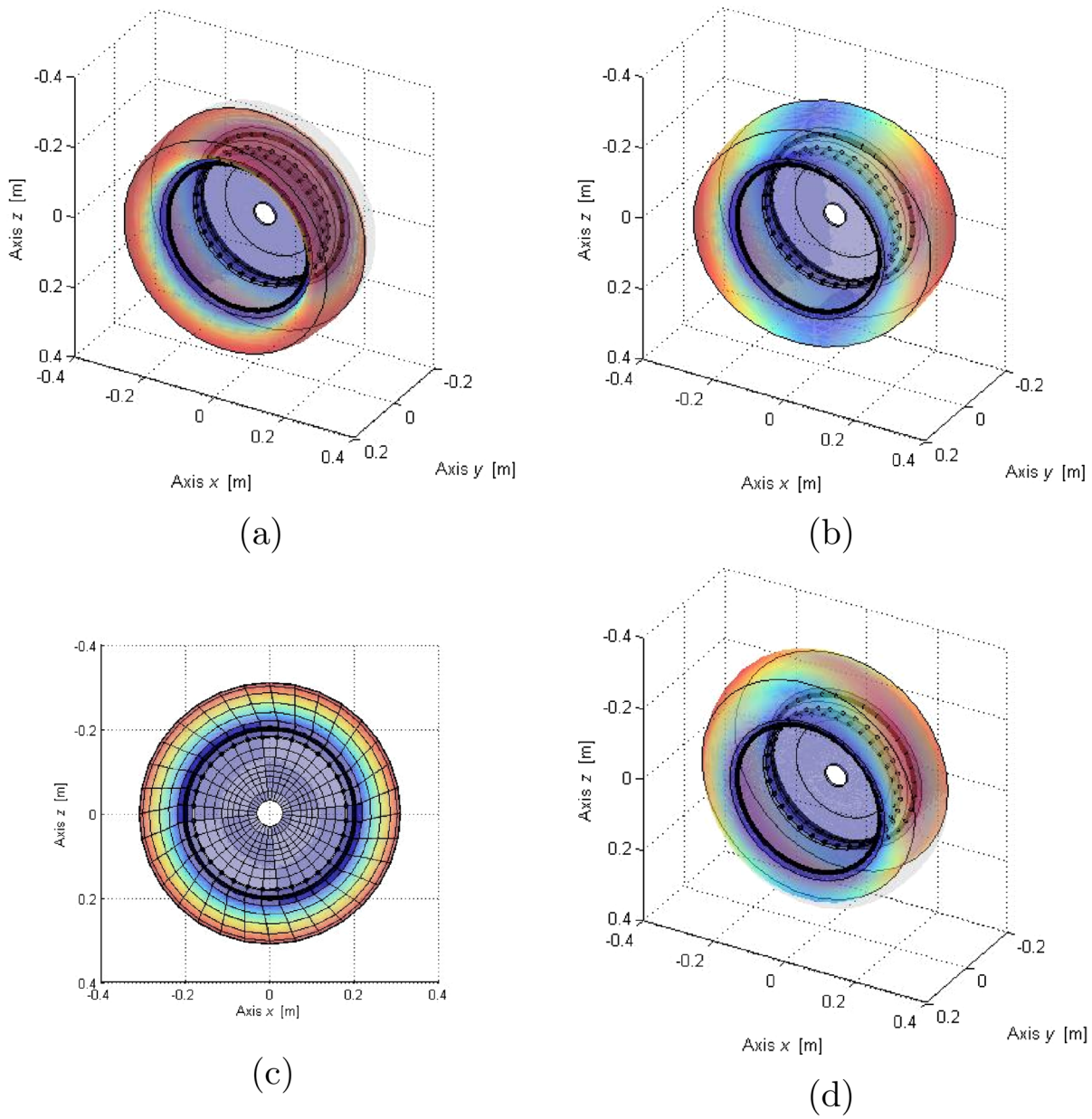

Fig. 4 Lateral (**a**), yaw/camber (**b**), torsion/spin (**c**) and vertical/longitudinal (**d**) modes of the car tyre finite-element model

the belt around that axis do not move (blue), while those far from the axis have the maximum displacement (red). As in the motorcycle tyre, there is another mode at the same frequency (the tyre is perfectly axial-symmetric) with the rotation axis perpendicular to the one depicted in Fig. 4b. Obviously, all rotation axes can be obtained by the combination of these two modes. The torsion/spin mode has a frequency of 72.8 Hz (damping 3.4%) and is shown in Fig. 4c. The portion of the belt close to the rim does not move (blue), while the portion around the rolling circumference has maximum displacement (red). Even in this case, belt distortions on the rolling portion of the belt are minimum, which moved like a rigid-ring. Finally, a vertical mode at 84.8 Hz (damping 2.8%) is shown in Fig. 4d. The portion of the belt on top (and bottom—not visible in the figure) have the maximum displacement (red), while the portions on the sides have smaller displacement (green). There is another mode at the same frequency (the tyre is perfectly axial-symmetric): it is the longitudinal mode. Vibration along each radial direction can be obtained by combination of these two modes. The finite-element model has many other (higher order) modes, which are not relevant in this work because they involve significant carcass distortion, and are thus not suitable to fit a rigid-ring model.

When obtaining the modal model, the minimum fitting correlations for lateral and tangential excitations is 99.9%, while the maximum error is 0.1%. The fitting of the radial excitation dataset provides correlations greater than 95% and errors smaller than 5% for both radial and tangential directions, with the exception of the tangential directions of node 1 and 9 (i.e. normal to the excitation), which have correlations of 71% and 70% and errors of 29% and 28%, respectively. The identified masses and inertias are reported in Tab. 2, where m_r is the mass/inertia that is associated to the rigid ring, m is the total mass/inertia of the belt, while the last column represents the ratio between the two inertias.

4 Experimental test

The experimental tests are carried out on a commercial motorcycle tyre, which has a mass of 10.7 kg, a camber/yaw moment of inertia of 0.45 kg m^2 and a spin moment of inertia of 0.86 kg m^2; see Fig. 5. The inertias have been obtained using a trifilar pendulum [49, 50] and the mass with a standard scale. The impact tests are carried out with the instrumented hammer PCB 086C03 and tri-axial accelerometers PCB 356A17 (which are attached to the tyre with standard wax, that makes it easy mounting and dismounting). A small (cube with length 15 mm and mass 5 g) impact block [39] has been glued to the tyre, in order to excite the node 1 along all three directions (otherwise only the vertical direction can be excited); see Fig. 5. The rim is fixed to a concrete pillion, that resembles an ideal fixed constraint. A roving-accelerometers approach is employed, since the mass of the accelerometers is much smaller than the mass of the belt (factor 1,000 between the two) and that moving the impact block is not practical. Each impact test is repeated five times, for averaging purposes. The acquisition length is 1 s (indeed the vibrations almost completely disappear after such length in the current application, and thus further extending the interval gives no additional information to the analysis) and the signals are sampled at 2048 Hz(thus assuring to potentially identify frequency up to 1 kHz). A rectangular windowing with length 5 ms is employed on the impact force signal, being the length of the typical impulse applied during the tests below such interval. No windowing was necessary on the acceleration signals, since the natural damping of the system is sufficient to damp the vibration within the acquisition period, without measuring only the sensor noise at the end of the measuring windows. The acquisition system consists of three NI-9234 modules mounted on a NI-9174 chassis.

Three excitation directions are considered, to give three sets of FRF. Each set is analysed separately. A

Table 2 Parameters of the car tyre rigid-ring model, extracted from the finite-element model

Mode	f_r	ζ_r	m_r	m	m_r/m
Lateral	51.4 Hz	4.7%	5.51 kg	8.05 kg	0.68
Camber/yaw	54.3 Hz	4.4%	0.26 kg m^2	0.35 kg m^2	0.74
Torsional/spin	72.8 Hz	3.4%	0.43 kg m^2	0.61 kg m^2	0.70
Vertical/longitudinal	84.8 Hz	2.8%	4.61 kg	8.05 kg	0.70

(a) (b)

Fig. 5 Experimental set-up for modal testing

lateral impulse (Fig. 5b top) is applied to excite predominantly the out-of-plane vibration modes of the tyre, such as lateral, yaw and camber modes. Vertical (Fig. 5b middle) and tangential (Fig. 5b bottom) impulses are applied to excite predominantly the in-plane modes. The vertical impulse mainly excites the vertical mode, while the tangential impulse mainly excites the torsional/spin mode. When inspecting the experimental FRF in the range 15–300 Hz, it is found that the modal model can be successfully obtained using $M = 7$ modes: the FRF generated by the lateral excitation are fit ted using three modes, namely lateral, camber/yaw and c-shape (which is a mode involving carcass distortion [36, 37]—not relevant in this work); the FRF generated by vertical excitation are fit ted using three modes, namely the radial mode and two more in-plane modes involving the carcass deflection (not relevant in this work); the FRF generated by tangential excitation are fit ted using one mode, namely the torsional/spin mode.

An example of FRF related to the lateral displacement of node 6 from the lateral excitation of node 1 is shown in Fig. 6a. The coherence is close to one across the whole frequency range. Three peaks are clearly visible in the experimental signal (solid line) at frequencies of 71.3 Hz (lateral mode), 103.5 Hz (camber mode) and 211 Hz (c-shape mode). The vertical dashed lines mark the resonances of the modes relevant to the rigid-ring model, i.e. lateral and camber modes only. The modal model fit ting of the experimental data is shown with a dashed line. The characteristics of the other FRF are similar. The fitting correlation is above 98% and the error is smaller than 2% when fitting the 48 FRF related to the lateral excitation, with the exception of the first node (excitation node) that has a correlation of 72% and an error of 29%.

An example of FRF related to the tangential displacement of node 3 from the tangential excitation of node 1 is shown in Fig. 6b. The coherence is close to one for frequencies between 50 Hz and 250 Hz. One peaks is clearly visible in the experimental signal (solid line) at a frequencies of 175 Hz (torsion/spin mode). The modal model fit ting of the experimental data is shown with a dashed line. A vertical dashed line marks the torsion resonance, since this mode is relevant for the rigid-ring model. The characteristics of the other FRF are similar. The fitting correlation is above 96% and error is less than 4% when fitting the 48 FRF related to the tangential excitation, with the exception of the first node that has a correlation of 84 and an error of 22%. It should be observed that the modal model focuses by design on the main torsional resonance of Fig. 6b. The higher-frequency dynamics can be neglected in this case, since their effect on the main resonance is negligible. On the contrary, in the case of Fig. 6a, also the higher frequency c-shape resonance has been included

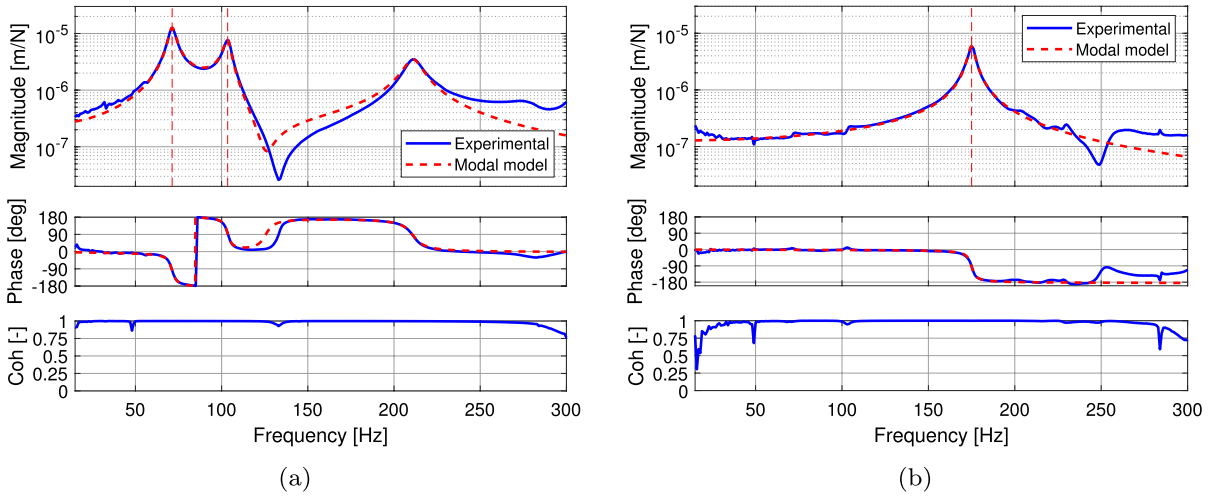

Fig. 6 Experimental FRF (solid) and fitted FRF (dashed): **a** lateral response of node 6 from lateral excitation in node 1 and **b** tangential response of node 3 from tangential excitation in node 1

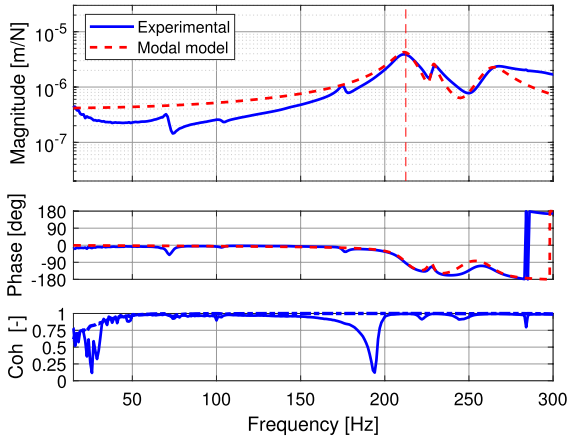

Fig. 7 Experimental FRF (solid) and fitted FRF (dashed): vertical response of node 2 from vertical excitation in node 1

in the modal model, because of its large magnitude and effect on the whole FRF.

An example of FRF related to the vertical motion of node 2 from the vertical excitation of node 1 is shown in Fig. 7. The acceleration in the vertical direction a_v is obtained by combining the radial a_r and tangential a_r accelerations as follows

$$a_{\mathrm{v}} = -a_{\mathrm{r}} \cos\theta + a_{\mathrm{t}} \sin\theta, \tag{8}$$

where θ is the angular position of the node, the angle is measured from the vertical direction (e.g. $\theta = 0$ for node 1 and $\theta = \pi/2$ for node 5); node 2 has $\theta = 22.5^o$. The coherence in the normal (radial) direction is close to one for frequencies above 50 Hz (dash-dot in Fig. 7 bottom). The coherence in the tangential direction is also close to one for frequencies above 50 Hz, with the exception of the visible dip in the range 175–200 Hz (solid line in Fig. 7 bottom). Three peaks are fitted from the experimental signal (solid line) at frequencies of 212 Hz (vertical mode), 229 Hz and 263 Hz. The latter two modes involve significant belt deflections—not relevant in this work. Therefore, only the radial mode has been marked with a dashed vertical line, since it is the only mode relevant for the rigid-ring model in this FRF. A small peak at 175 Hz is also visible (torsion mode, which is better excited with tangential excitation, see Fig. 6b), together with a small peak at 71 Hz (lateral mode, which is better excited with lateral excitation, see Fig. 6a). Finally, a small perturbation in the FRF at 102 Hz is visible, likely due to the yaw/camber mode (better excited with lateral excitation, see Fig. 6a). The modal model fit ting of the experimental data is shown with a dashed line. In the radial direction the fitting correlation is above 55% and the error is smaller than 53%, while in the tangential direction the fitting correlation is above 49% and the error is smaller than 53%, with the exception of the first node which has a correlation of 16% and an error of 93%. In general, the fitting correlation of the vertical mode are much more

variable than those related to the lateral and tangential excitations, and the errors larger.

It is worth stressing that the tyre under investigation has a c-shape mode at 211 Hz (Fig. 6), which is very close to the 212 Hz (Fig. 7) of the vertical mode. The c-shape mode is predominantly out-of-plane, with minimum in-plane components. On the contrary, the vertical mode is predominantly in-plane, with minimum out-of-plane components. This is a quite challenging condition, since the inspection of a limited number of FRF, i.e. without the inspection of the three-dimensional mode shape obtained by the fit ting of the modal model, may lead to the assumption that the peaks at 211 Hz and 212 Hz belong to the same mode.

The shapes of the modes identified are shown in Figs. 8, 9, 11, both in terms of compass diagrams and a three-dimensional representations, while the natural frequencies and damping ratios are summarized in Tab. 3. In the compass diagram there is one arrow per node: the magnitude is related to the length of the arrow, while the phase is related to the angle of the arrow. As usual in modal analysis, only the ratio between magnitudes and the relative angles matter. In the three-dimensional representation the magnitude of the complex eigenvector components are shown. In most cases, all components are almost in-phase or in phase-opposition.

Figure 8a shows the compass plot of the lateral displacements of the lateral mode. All nodes move laterally almost exactly in-phase, with nearly identical magnitude, thus supporting the rigid-ring model approach. The dashed arrow represents the rigid-ring fit ting. Figure 8b shows the three-dimensional mode shape of the lateral mode, which highlights that the in-plane components are negligible, and the experimental deflection (stars) is very close to a pure lateral translation.

Figure 9a shows the compass plot of the rotational displacement of the camber mode, which are computed from the ratio of the lateral displacement of each node and its distance from the camber axis. Even in this case all the rotational components are almost exactly in phase, the dashed line being the rigid-ring fit ting. The three-dimensional representation in Fig. 9b shows that in the camber mode half of the nodes move laterally almost exactly in-phase (those above the x axis), while the others (those below the

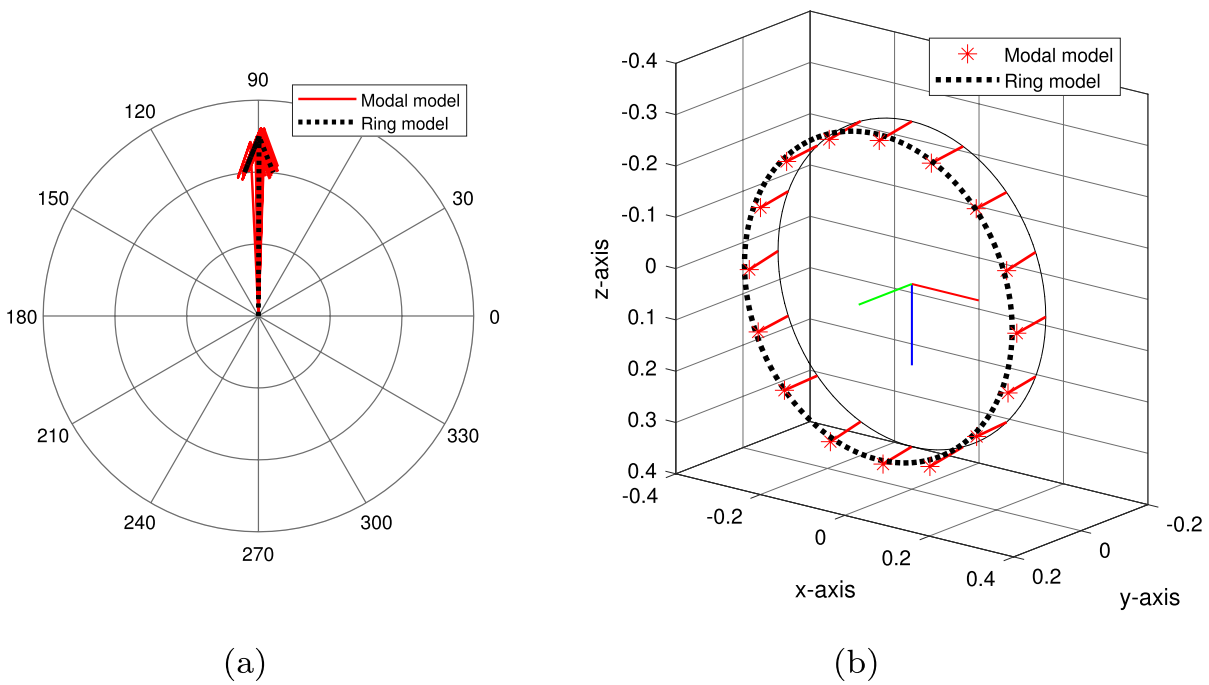

Fig. 8 Lateral mode: modal model from experiments versus rigid-ring fit. Vertical displacements (**a**) and three-dimensional representation (**b**)

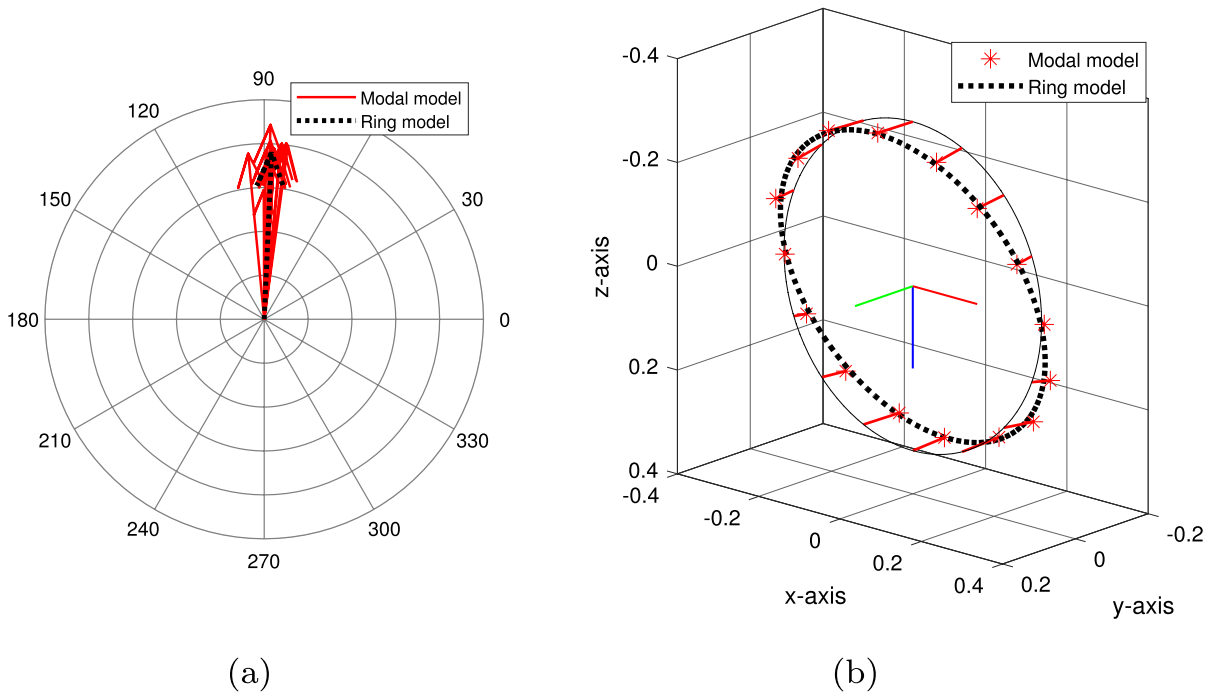

Fig. 9 Camber/yaw mode: modal model from experiments versus rigid-ring fit. Vertical displacements (**a**) and three-dimensional representation (**b**)

x axis) move in phase-opposition. The result supports the rigid-ring modelling approach. Obviously, if the lateral excitation is moved from node 1 to node 5 or 13, the yaw mode is revealed (instead of the camber), with a rotation axis almost coincident with the *z* axis. Therefore, we will refer to this mode with the name camber/yaw mode.

Figure 10a displays the compass plot of the torsion/spin mode in terms of the tangential displacement of the nodes. All the nodes move tangentially almost exactly in-phase with almost identical magnitude. Again, the dashed line shows the rigid-ring fit ting. Figure 10b shows the three-dimensional representation of the mode, which highlights negligible components out-of-plane. This again supports the rigid-ring modelling approach.

Figure 11a shows the compass plot of the vertical mode. The larger magnitudes are those associated to the nodes farther from the *x* axis, i.e. top and bottom. The nodes on top of the tyres appear to have larger displacements with respect to those on the bottom. The displacements are still quite in phase, although less than what has been observed for the lateral, yaw/camber and torsion/spin modes. Figure 11b shows that there are also significant components in the longitudinal direction, and some component in the lateral direction, in addition to those in the vertical direction. Some belt deflections are visible. This is not surprising because the frequency of this mode is much higher than those of the lateral, camber/yaw and spin. Of course, if the vertical excitation in node 1 is changed to a longitudinal excitation o nodes 5 or 13 the longitudinal mode is obtained (instead of the vertical). Therefore, we will refer to this mode with the name radial mode.

Finally, the masses associated to each mode are identified, with the procedure explained in Sect. 2, and the results are summarized in Tab. 3, while the mean FRF are shown in Fig. 12.

Figure 12a shows the FRF associated to the lateral vibration mode extracted from the modal model (solid lines) and the ring-model FRF (dashed line) obtained by fit ting. The curves are almost indistinguishable from one another. This is expected since the mode shape analysis above confirmed that the lateral mode is indeed a rigid-ring mode. The mass associated to the lateral mode of the ring is 67% of the mass of the whole belt. It was 81% in the case of

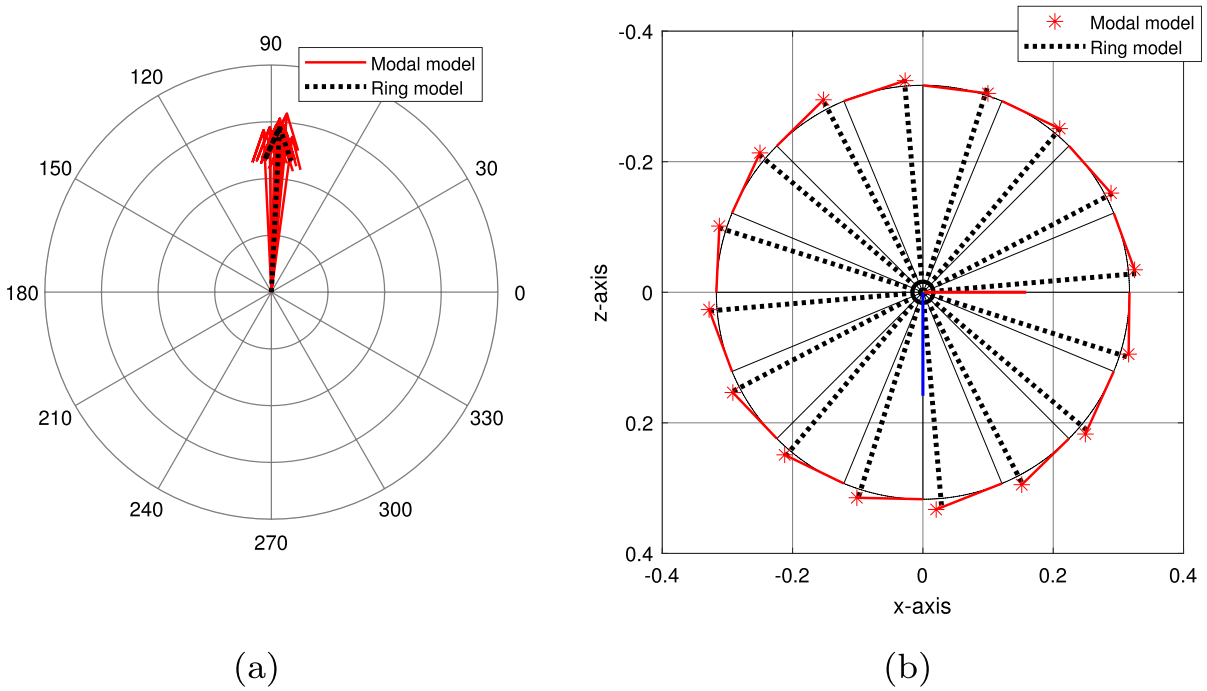

Fig. 10 Torsion/spin mode: modal model from experiments versus rigid-ring fit. Vertical displacements (**a**) and three-dimensional representation (**b**)

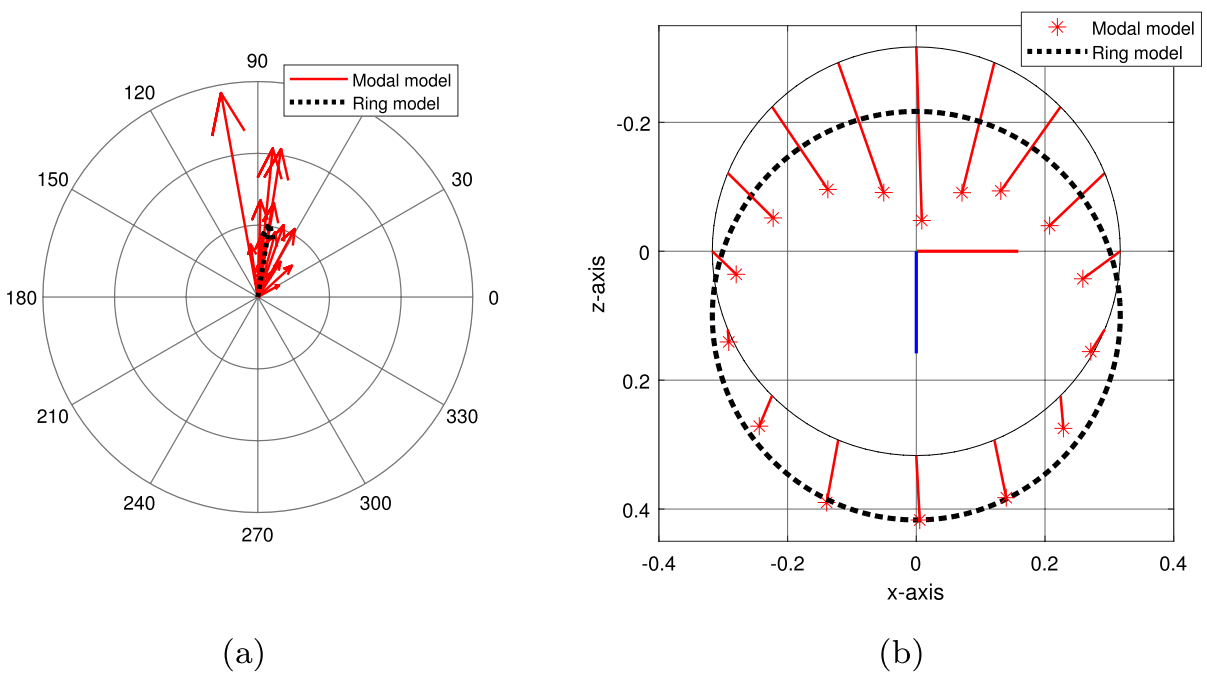

Fig. 11 Vertical/radial mode shape: modal model from experiments versus rigid-ring fit. Vertical displacements (**a**) and three-dimensional representation (**b**)

Table 3 Experimental analysis

Mode	f_r	ζ_r	m_r	m	m_r/m
Lateral	71.3 Hz	2.77%	7.21 kg	10.7 kg	0.67
Camber/yaw	103.5 Hz	1.79%	0.35 kg m^2	0.45 kg m^2	0.78
Torsional/spin	175.0 Hz	1.12%	0.66 kg m^2	0.86 kg m^2	0.77
Vertical/longitudinal	212.2 Hz	3.15%	4.30 kg	10.7 kg	0.40

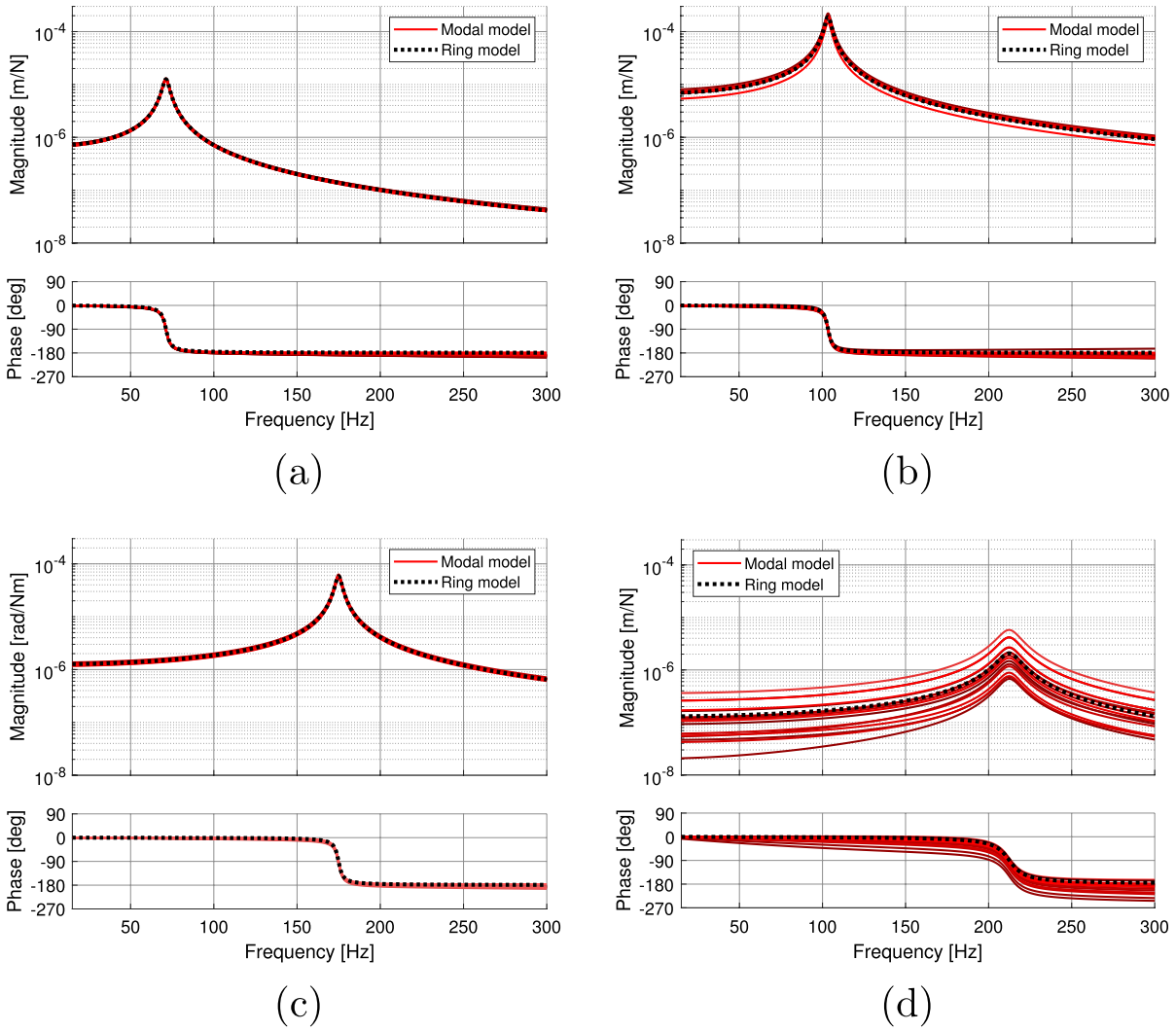

Fig. 12 Lateral (**a**), camber (**b**), spin (**c**) and radial (**d**) mean FRF

the finite-element model in Sect. 3, while 75% is the value suggested in [2].

Figure 12b shows the FRF associated to the camber/yaw mode extracted from the modal model (solid lines) and the ring-model FRF (dashed line) obtained by fit ting. Even in this case the curves are almost indistinguishable from one another, as the mode shape analysis above suggested. The inertia associated to the camber mode of the ring is 78% of the inertia of the whole belt. It was 87% in the case of

the finite-element model in Sect. 3, while 85% is the value suggested in [2].

Figure 12c shows the FRF associated to the torsional/spin mode extracted from the modal model (solid lines) and the ring-model FRF (dashed line) obtained by fit ting. Once again the curves are almost indistinguishable from one another: the mode is indeed well represented by a rigid-ring motion. The inertia associated to the spin mode of the ring is 77% of the inertia of the whole belt. It was 80% in the case of the finite-element model in Sect. 3, while 85% is the value suggested in [2].

Figure 12d shows the FRF associated to the vertical mode extracted from the modal model (solid lines) and the ring-model FRF (dashed line) obtained by fit ting. In this case different FRF are visible, since the different locations have different displacements and (slightly) different phases. The mass associated to the vertical mode of the ring is 40% of the mass of the whole belt. It was again 40% in the case of the finite-element model in Sect. 3, while 75% is the value suggested in [2].

The inspection of the mode shapes in Fig. 8-11 suggest that a classical damping assumption could be enforced during the modal model fit ting, since the actual shapes are almost real (i.e. their components are either in phase or in phase opposition). In practice, this is a good assumption for the lateral, camber/yaw and torsional mode only, while it is not for the vertical mode, which exhibits significant phase lags between the different components. As a result, when repeating the mass identification procedure starting from the real mode shapes, instead of the complex mode shapes, the changes in the values of the masses and inertias identified are negligible for the lateral, camber/yaw and torsional modes, while it is more significant for the vertical mode (in this case the identified mass increases to the 44% of the belt mass).

5 Remarks

5.1 Numerical versus experimental tests on the motorcycle tyre

The proposed identification procedure (Sect. 2) has been successfully applied both to a numerical motorcycle tyre model (Sect. 3) and to a real 180/65–16 motorcycle tyre (Sect. 4). The reason for the application to the numerical tyre model, resembling the characteristic of the real tyre, is to confirm on a ideal environment the trends observed with the experimental campaign and support the interpretation of the results and the extraction of the ring-model parameters.

In particular, both the motorcycle tyre numerical and the experimental analyses are in agreement in terms of modal shape and vibrating mass ratio and confirm that the mass of the ring associated to the lateral motion is considerably different from the mass associated to the longitudinal/vertical directions. Indeed, in the latter mode (in-plane mode), there is a portion of belt that is not moving significantly, while in the case of the lateral mode (out-of-plane mode) most of the belt moves. The quantification of the vibrating mass follows from the fit of the FRFs with the SDOF rigid-ring model. The consequence is that, when it comes to the practical implementation of the rigid-ring model, a choice needs to be made between the two masses, since a single mass value can be assigned to the ring body, e.g. in a multibody environment. As expected, all the ratios of the vibrating mass to the whole belt mass are smaller than one, since the portion of the belt in contact with the rim does not participate in the vibration, as also intuition suggests.

There is not the same problem with the inertias. The inertia associated to spin motion (in-plane) can be different from that of the yaw/camber (out-of-plane) motion. Indeed, when it comes to the practical implementation of the rigid-ring model, one can assign different inertias associated to the spin and yaw/camber directions. As expected, similarly to the masses, also all the ratios of the vibrating inertia to the whole belt inertia are smaller than one (the result follows from the fit of the FRFs with the SDOF ring-model).

5.2 Rigid-ring assumption

The rigid-ring model basically aims to fit (at mid-low frequencies) the behaviour of the tyre using six DOFs, namely the three translations and three rotations of the belt with respect to the rim. The frequencies of the six vibration modes of the rigid ring match the frequencies of the six corresponding vibration modes of the tyre, by design. The mode shapes of the rigid-ring mode closely resemble those of the tyre,

as shown in the compass plots in Sect. 4. Another comparison can be carried out using the modal assurance criterion (MAC) [51–53], which is an approach often used to quantitatively compare the experimentally identified mode shape against the corresponding numerical mode shape (in this case those of the rigid-ring model).

The complex eigenvector MAC formulation is used in this work. Given two sets of complex eigenvectors $\boldsymbol{\psi}_{\mathrm{A}}$ and $\boldsymbol{\psi}_{\mathrm{B}}$, the MAC value between the r^{th} eigenvector of the first set and the q^{th} eigenvector of the second set is calculated as follows

$$\mathrm{MAC}(r,q) = \frac{|\boldsymbol{\psi}_{\mathrm{A,r}}^{\mathrm{T}} \boldsymbol{\psi}_{\mathrm{B,q}}^{*}|^2}{\left(\boldsymbol{\psi}_{\mathrm{A,r}}^{\mathrm{T}} \boldsymbol{\psi}_{\mathrm{A,r}}^{*}\right)\left(\boldsymbol{\psi}_{\mathrm{B,q}}^{\mathrm{T}} \boldsymbol{\psi}_{\mathrm{B,q}}^{*}\right)}, \tag{9}$$

where the superscript * identifies the complex conjugate.

The comparison between the rigid-ring and experimental eigenvectors is reported in Fig. 13a. The MAC is greater than 0.98 for the lateral, yaw/camber and torsion modes, while it is 0.51 for the radial mode. The off-diagonal terms of the MAC are below all below 0.01. The analysis confirm that the lateral, yaw and torsional mode are well represented by a rigid-ring model, while the result of the radial mode needs some comment.

The rigid-ring radial mode is purely in-plane, while the experimentally measured radial mode has some out-of-plane component. Once the out-of-plane components are neglected, the MAC increases from 0.51 to 0.54. It is concluded that this is not the main source of difference in the mode shape. The rigid-ring radial mode is purely vertical, while the experimentally measured radial mode also has some longitudinal component. Once the experimental mode shape are restricted to the vertical components only, the MAC rises from 0.54 to 0.65. Finally, one can think of removing from the MAC calculation the top node (number 1 in Fig. 2), which coincides with the impact point and shows a magnitude a bit larger than the others: in this case the MAC rises to 0.71. There still is a difference between the experimental and rigid-ring mode shape.

This issue is further clarified in Fig. 14, which compares the magnitude of the vertical (top plot) and horizontal (bottom plot) displacements of the nodes along the tyre belt in the case of the experimental radial mode (modal model), rigid-ring radial mode and finite-element (FE) radial mode. The finite-element model is introduced to confirm that the observed shape is not related to a measurement problem, but is indeed a typical behaviour of the tyre. From the modes comparison it is clear that also the FE mode shares the same pattern of

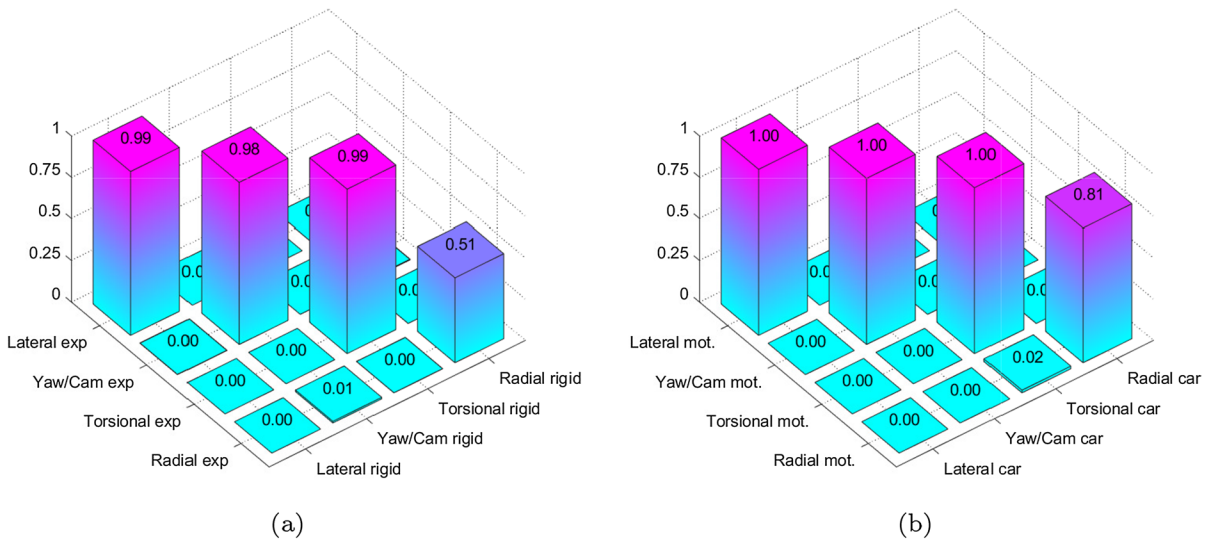

Fig. 13 MAC of the rigid-ring modes versus motorcycle tyre experimental modes (**a**) and motorcycle tyre numerical modes versus car tyre modes (**b**)

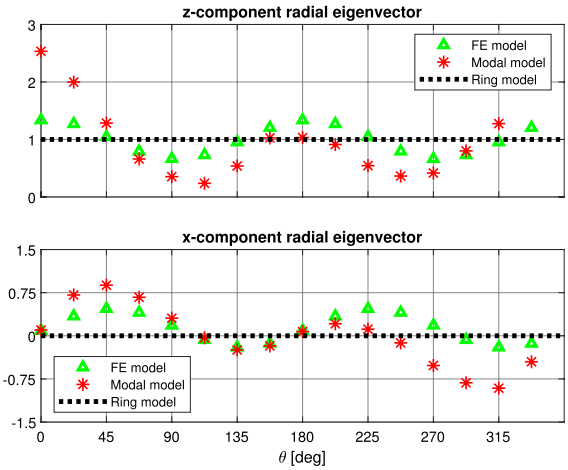

Fig. 14 Motorcycle vertical mode shape: vertical (top) and horizontal (bottom) components at the different angular (θ) locations

the experimental model for the vertical displacement of the nodes, with the top ($\theta = 0^o$) and bottom ($\theta = 180^o$) nodes moving more than the nodes around the height of the wheel hub ($\theta = 90^o$ and $\theta = 270^o$). However, in the case of the modal model, the bottom points (around $\theta = 180^o$) are moving less than the top points (around $\theta = 0^o$). As regards the longitudinal displacements, the shape of the modal model is similar to the one of FE model, but the magnitude is larger. It is concluded that the main difference in the MAC is related to the asymmetric shape in the vertical direction and excessive magnitude in the longitudinal shape. The relative importance can be deduced when comparing the shape of the shape of the mode in the FE model and the ring model. The MAC between the two models is 0.88, and rises to 0.95 when the computation is performed on the vertical motion only.

The discussion shows that the representation of the dynamics of a real tyre by a rigid-ring model could led to some approximation of the lower-order dynamics. However, this need not be always the case. Indeed, with the car tyre considered in this work, the radial modes do not have the asymmetry that observed in the motorcycle radial modes. Indeed, when applying MAC to compare the car radial mode against the rigid-ring radial mode, a value of 0.98 is obtained, confirming the very good fit of the rigid-ring assumption on this tyre.

5.3 Motorcycle tyre versus car tyre

The proposed identification procedure (Sect. 2) has been successfully applied to numerical tyre models (Sect. 3) which differ significantly in terms of cross-section and aspect ratio. The two models show different natural frequency and damping ratios. However, both their low-frequency modes show the typical modal shapes of the rigid-ring model. Their eigenvectors thus fit equally well against a rigid translation of the outer belt, with the exception of the radial mode, which need some additional considerations. The car tyre shows an almost rigid radial mode, which thus provide a MAC of 0.98 when compared against the rigid-ring shape. On the contrary, the motorcycle tyre, whose behaviour has also been confirmed by the experimental analysis, exhibits moderate deflection of the belt, which departs from the ideal rigid-ring shape and lead to MAC value of 0.88.

As regards the mass ratios, there is a quite a good agreement between the results obtained with the car and motorcycle tyres, especially when it comes to the lateral, camber and torsional modes, which show ratios in between 68% and 87%. On the contrary, a noticeable difference is observed in the belt masses associated to the radial mode, which is way higher in the car tyre (70%) than in the motorcycle tyre (40%). The reason of this difference is related to the different mode shapes, which are compared in Fig. 15. Indeed, the higher belt mass involved in the radial vibration obtained with the car tyre is related to a mode shape that engages in-phase motion of the the whole belt. On the other hand, the motorcycle tyre shows a radial mode with a reduced engagement of the outer belt, showing, as confirmed by the experimental analysis in Fig. 11, a peak of the belt motion in the top and bottom sides, and a minimum in the lateral sides.

The MAC between the motorcycle and car numerical mode shapes is shown in Fig. 13b. It is confirmed that the all the low-frequency modes are nearly identical, with the exception of the radial mode, whose MAC reduces to 0.81 because of the differences described above and also highlighted in Fig. 15.

5.4 Multiplicity and axial-symmetry

Due to tyre axial-symmetry, the eigenproblem solution produces yaw and camber modes with the same frequency (multiplicity two) and vertical and

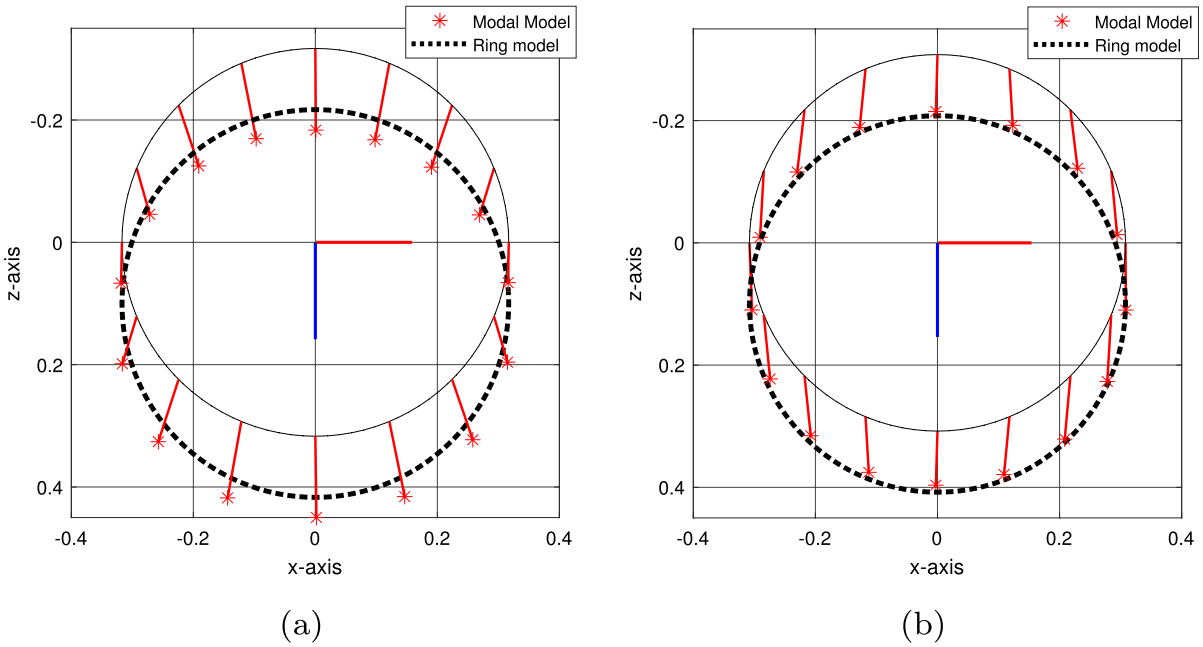

Fig. 15 Comparison of motorcycle tyre (**a**) and car tyre (**b**) vertical/radial mode shape

longitudinal modes with the same frequency (multiplicity two) [54]. Examples of coincident modes in the case of car and bicycle wheels are analysed e.g. in [55, 56]. Although there is orthogonality between the rotation axes of the yaw/camber modes and between the displacement direction of the vertical/longitudinal modes, they are not necessarily aligned to the global reference frame. A specific camber/yaw mode is obtained by a linear combination of the two modes extracted from the eigenproblem [55]. The same applies to any radial mode, which is obtained by a linear combination of the two modes extracted. For the comparison between the experimental and FE radial modes, the two numerical eigenvectors are linearly composed in order to create a mode shape aligned to the direction of the mode obtained experimentally.

6 Conclusion

A procedure for the identification of the dynamic parameters of the rigid-ring tyre model has been devised. The approach is based on experimental modal analysis and focuses on the vibration modes of an unloaded tyre fixed to the ground through its rim. When comparing against other methods reported in the literature, the proposed method allows for the full characterization of both in-plane and out-of-plane dynamics, thus leading also to the quantification of the masses and inertia associated to the rigid-ring body (which are generally lower than the mass and inertia of the tyre), while requiring only standard vibrational analysis equipment (which is not the case of many approaches reported in the literature). Both the numerical and experimental analyses carried out confirm that most of the low-frequency modes are characterised by minimum distortion of the tyre belt, that can thus be considered a rigid ring body. The modes identified on the motorcycle tyre are in the range 70–220 Hz, while on the car tyre are in the range 51–85 Hz. At lower frequencies there are the lateral and yaw/camber modes, while at higher frequencies there are the vertical/longitudinal and spin/torsion modes. It is found that the mass associated to the vertical mode is not necessarily close to the mass associated to the lateral mode. Indeed, while the car tyre shows a vertical-mode mass (70%) close to the lateral-mode mass (68%), the motorcycle tyre shows a much lower vertical mass (40%) than lateral mass (81%). The significant difference is related to the motorcycle vertical mode shape, which departs from the ideal rigid-ring shape. On the contrary, both the

motorcycle and car tyres show an inertia associated to the camber/yaw modes (74–87% of the tyre inertia) that is similar to the one associated to the torsion mode (70–80% of the tyre inertia).

Funding Open access funding provided by Università degli Studi di Padova within the CRUI-CARE Agreement.

Declarations

Conflict of interest The authors declare that they have no conflict of interest.

References

1. Limebeer DJN, Massaro M (2018) Dynamics and optimal control of road vehicles. Oxford University Press, Oxford
2. Pacejka HB (2012) Tire and vehicle dynamics, 3rd edn. Butterworth Heinemann, Oxford
3. Cossalter V (2006) Motorcycle dynamics, 2nd Edn. Lulu.com
4. Guiggiani M (2014) The science of vehicle dynamics: handling, braking, and ride of road and race cars. Springer, Berlin
5. Gillespie TD (1992) Fundamentals of vehicle dynamics. SAE International
6. Massaro M, Limebeer DJN (2021) Minimum-lap-time optimisation and simulation. Veh Syst Dyn 59(7):1069–1113. https://doi.org/10.1080/00423114.2021.1910718
7. Lovato S, Massaro M, Limebeer DJN (2021) Curved-ribbon-based track modelling for minimum lap-time optimisation. Meccanica 56:2139–2152. https://doi.org/10.1007/s11012-021-01387-3
8. Marconi E, Massaro M (2022) Optimal recovery manoeuvres of racing motorcycles. Meccanica 57(2):457–472. https://doi.org/10.1007/s11012-021-01454-9
9. Hirschberg W, Rill H, Weinfurter G (2007) Tire Model TMeasy. Veh Syst Dyn 45(S1):101–119. https://doi.org/10.1080/00423110701776284
10. Février P, Fandard G (2014) A new thermal and mechanical tire model for handling simulation. VDI-Berichte 2007:261–275
11. Pacejka HB, Besselink IJM (1997) Magic formula tyre model with transient properties. Veh Syst Dyn 27(S1):243–249. https://doi.org/10.1080/00423119708969658
12. Romano L, Timpone F, Bruzelius F, Jacobson B (2022) Analytical results in transient brush tyre models: theory for large camber angles and classic solutions with limited friction. Meccanica 57(1):165–191. https://doi.org/10.1007/s11012-021-01422-3
13. TNO Automotive (2013) MF-Tyre/MF-Swift 6.2 Equation manual. Delft-Tyre
14. Schmeitz AJC, Besselink IJM, Jansen STH (2007) Tno mf-swift. Veh Syst Dyn 45(sup1):121–137
15. Zegelaar PWA, Pacejka HB (1996) The in-plane dynamics of tyres on uneven roads. Veh Syst Dyn 25(sup1):714–730. https://doi.org/10.1080/00423119608969231
16. Oertel C, Fandre A (2009) Tire model RMOD-K 7 and misuse load cases. SAE 20 Apr 2009
17. Gipser M (2007) Ftire—the tire simulation model for all applications related to vehicle dynamics. Veh Syst Dyn 45(sup1):139–151. https://doi.org/10.1080/00423110801899960
18. Gallrein A, Bäcker M (2007) Cdtire: a tire model for comfort and durability applications. Veh Syst Dyn 45(sup1):69–77. https://doi.org/10.1080/00423110801931771
19. Farroni F, Sakhnevych A, Timpone F (2019) A three-dimensional multibody tire model for research comfort and handling analysis as a structural framework for a multi-physical integrated system. Proc Inst Mech Eng D J Autom Eng 233(1):136–146. https://doi.org/10.1177/0954407018799006
20. Farroni F, Giordano D, Russo M, Timpone F (2014) TRT: thermo racing tyre a physical model to predict the tyre temperature distribution. Meccanica 49(3):707–23
21. Braghin F, Cheli F, Melzi S, Resta F (2006) Tyre wear model: validation and sensitivity analysis. Meccanica 41(2):143–156. https://doi.org/10.1007/s11012-005-1058-9
22. Dubois G, Cesbron J, Yin H, Anfosso-Lédée F (2012) Numerical evaluation of tyre/road contact pressures using a multi-asperity approach. Int J Mech Sci 54(1):84–94. https://doi.org/10.1016/j.ijmecsci.2011.09.010
23. Jenkins JT (1980) A theoretical determination of the contact pressure across the central meridian of a belted radial tire. Int J Mech Sci 22(9):575–581. https://doi.org/10.1016/0020-7403(80)90019-3
24. Baranowski P, Malachowski J, Mazurkiewicz L (2016) Numerical and experimental testing of vehicle tyre under impulse loading conditions. Int J Mech Sci 106:346–356. https://doi.org/10.1016/j.ijmecsci.2015.12.028
25. Moore DF (1967) A theory of viscous hydroplaning. Int J Mech Sci 9(12):797–810. https://doi.org/10.1016/0020-7403(67)90008-2
26. Grogger H, Weiss M (1997) Calculation of the hydroplaning of a deformable smooth-shaped and longitudinally-grooved tire. Tire Sci Technol 25(4):265–287. https://doi.org/10.2346/1.2137544
27. Yam LH, Guan DH, Zhang AQ (2000) Three-dimensional mode shapes of a tire using experimental modal analysis.

Exp Mech 40(4):369–375. https://doi.org/10.1007/BF02326482
28. Zegelaar PWA, Gong S, Pacejka HB (1994) Tyre models for the study of in-plane dynamics. Veh Syst Dyn 23(sup1):578–590. https://doi.org/10.1080/00423119308969542
29. Zegelaar P (1997) Modal analysis of tire in-plane vibration. SAE Technical Papers
30. Maurice JP, Zegelaar PWA, Pacejka HB (1998) The influence of belt dynamics on cornering and braking properties of tyres. Veh Syst Dyn 29(sup1):299–311. https://doi.org/10.1080/00423119808969566
31. Bruni S, Cheli F, Resta F (1997) On the identification in time domain of the parameters of a tyre model for the study of in-plane dynamics. Veh Syst Dyn 27(sup001):136–150. https://doi.org/10.1080/00423119708969650
32. Schmeitz AJC, Versteden WD (2009) Structure and parameterization of mf-swift, a magic formula-based rigid ring tire model. Tire Sci Technol 37(3):142–164. https://doi.org/10.2346/1.3138768
33. Saemann E-U, Ropers C, Morkholt J, Omrani A (2003) Identification of tire vibrations. In: SAE 2003 noise & vibration conference and exhibition. SAE International
34. Patil K, Baqersad J, Behroozi M (2017) Experimental modal analysis on a tyre—lessons learned. Int J Veh Noise Vib 13(3–4):200–215. https://doi.org/10.1504/IJVNV.2017.089507
35. Geng Z, Popov A, Cole D (2007) Measurement, identification and modelling of damping in pneumatic tyres. Int J Mech Sci 49(10):1077–1094. https://doi.org/10.1016/j.ijmecsci.2007.03.004
36. Doria A, Taraborrelli L, Urbani M (2014) A modal approach for the study of the transient behavior of motorcycle and scooter tires. In: ASME international design engineering technical conferences and computers and information in engineering conference
37. Doria A, Taraborrelli L (2016) Out-of-plane vibrations and relaxation length of the tyres for single-track vehicles. Proc Inst Mech Eng D J Automob Eng 230(5):609–622
38. Diaz CG, Kindt P, Middelberg J, Vercammen S, Thiry C, Close R, Leyssens J (2016) Dynamic behaviour of a rolling tyre: experimental and numerical analyses. J Sound Vib 364:147–164. https://doi.org/10.1016/j.jsv.2015.11.025
39. SAE International (2017) Modal testing and identification of lower order tire natural frequencies of radial tires
40. Ewins DJ (2000) Modal testing: theory, practice and application, 2nd edn. Mechanical engineering research studies. Engineering dynamics series. Research Studies Press, Baldock
41. Silva JMM (1999) Modal analysis and testing/edited by Julio M. M. Silva and Nuno M. M. Maia, NATO ASI series. Series E, Applied sciences, Kluwer, published in cooperation with NATO scientific affairs division, Dordrecht
42. Peeters B, Van der Auweraer H, Guillaume P, Leuridan J (2004) The PolyMAX frequency-domain method: a new standard for modal parameter estimation? Shock Vib 11(3):395–409
43. Bonisoli E (2023) Lupos: Lumped parameters open source fem code, Politecnico di Torino, Department of Mechanical and Aerospace Engineering, Torino, Tutorial v. 16 Jan 2023
44. Bonisoli E, Dimauro L, Venturini S (2023) Lupos: open-source scientific computing in structural dynamics. In: Proceedings of the 41st IMAC
45. Caughey T (1960) Classical normal modes in damped linear dynamic systems. J Appl Mech Trans ASME 27(2):269–271. https://doi.org/10.1115/1.3643949
46. Caughey T, O'Kelly M (1965) Classical normal modes in damped linear dynamic systems. J Appl Mech Trans ASME 32(3):583–588. https://doi.org/10.1115/1.3627262
47. Prandina M, Mottershead J, Bonisoli E (2009) An assessment of damping identification methods. J Sound Vib 323(3–5):662–676. https://doi.org/10.1016/j.jsv.2009.01.022
48. Bonisoli E, Delprete C, Rosso C (2009) Proposal of a modal-geometrical-based master nodes selection criterion in modal analysis. Mech Syst Signal Process 23(3):606–620. https://doi.org/10.1016/j.ymssp.2008.05.012
49. Korr AL, Hyer P (1962) A trifilar pendulum for the determination of moments of inertia
50. SAE J2717: Tests to define tire size (geometry), mass, inertias (2018)
51. Allemang RJ, Brown DL (1982) A correlation coefficient for modal vector analysis. In: 1st IMAC, pp 110–116
52. Allemang RJ (2003) The modal assurance criterion—twenty years of use and abuse. Sound Vib. 37(8):14–21
53. Pastor M, Binda M, Harčarik T (2012) Modal assurance criterion. Procedia Eng 48:543–548. https://doi.org/10.1016/j.proeng.2012.09.551
54. Bonisoli E, Brino M, Delprete C (2019) Numerical-experimental comparison of a parametric test-rig for crossing and veering phenomena. Mech Syst Signal Process 128:369–388. https://doi.org/10.1016/j.ymssp.2019.03.039
55. Bonisoli E, Marcuccio G, Venturini S (2021) Interference fit estimation through stress-stiffening effect on dynamics. Mech Syst Signal Process 160:107919. https://doi.org/10.1016/j.ymssp.2021.107919
56. Bonisoli E, Vella AD, Venturini S (2022) Uncertainty effects on bike spoke wheel modal behaviour, in: Model Validation and Uncertainty Quantification. In: 40th IMAC, conference and exposition on structural dynamics 2022, vol 3. https://doi.org/10.1007/978-3-031-04090-0_13